Draft version.

Compton telescope with coded aperture mask: Imaging with the INTEGRAL/IBIS Compton mode

M. Forot[1], P. Laurent[1], F. Lebrun[1] and O. Limousin[1]

mforot@cea.fr

ABSTRACT

Compton telescopes provide a good sensitivity over a wide field of view in the difficult energy range running from a few hundred keV to several MeV. Their angular resolution is, however, poor and strongly energy dependent. We present a novel experimental design associating a coded mask and a Compton detection unit to overcome these pitfalls. It maintains the Compton performance while improving the angular resolution by at least an order of magnitude in the field of view subtended by the mask. This improvement is obtained only at the expense of the efficiency that is reduced by a factor of two. In addition, the background corrections benefit from the coded mask technique, i.e. a simultaneous measurement of the source and background. This design is implemented and tested using the IBIS telescope on board the INTEGRAL satellite to construct images with a $12'$ resolution over a 29x29 field of view in the energy range from 200 keV to a few MeV. The details of the analysis method and the resulting telescope performance, particularly in terms of sensitivity, are presented.

Subject headings: gamma rays:observation – instrument:Compton – telescopes

1. Introduction

The development of Compton telescopes began in the 1970's with balloon flights (Schönfelder & Lichti 1973; Herzo et al. 1975; Lockwood et al. 1979) and culminated with the flight of COMPTEL (Schönfelder et al. 1993) on board the Compton Gamma Ray Observatory (CGRO). COMPTEL has shown for more than 9 years the capabilities of a Compton

[1]Service d'Astrophysique, CEA Saclay, 91191, GIF sur YVETTE, France

telescope to image the sky between 1 and 30 MeV thanks to the Compton kinematics information (Boggs & Jean 2000). The study of astrophysical sites of nucleosynthesis, as illustrated by the first ^{26}Al skymap (Diehl et al. 1995), largely progressed with the COMPTEL data. On the other hand, COMPTEL barely achieved a 5 deg (FWHM) angular resolution at 1 MeV. Future Compton telescopes could benefit from the very significant detector progress, particularly in the semiconductor domain, to improve the spectral resolution, thus the angular resolution (Limousin 2003). The latter is, however, intrinsically limited by what is referred to as the electron Doppler broadening which results from the fact that the scattering electron in a detector is bound. This limits the angular resolution to about 5 deg at 511 keV in the best case (Zoglauer & Kanbach 2003).

One way to overcome this limitation is to adjoin a coded aperture (mask) to a Compton telescope. This design, which has never been used for gamma-ray space telescopes, maintains the advantages of a Compton telescope (high-energy response, low background, wide field of view) over most of the wide field of view, but it adds the coded mask imaging properties (angular resolution, background subtraction) in the solid angle subtended by the mask. Indeed, in a coded mask system, source and background are measured simultaneously and the energy independent angular resolution is more than one order of magnitude better than in classical Compton telescopes. With Coded Aperture Compton Telescopes (hereafter CACT), we can obtain low background images in the 200 keV–10 MeV energy range, with an angular resolution better than a fraction of degree (e.g. 10 arcmin).

Anyway, a CACT has generally a lower efficiency than a classical coded mask telescope with, for instance, a thicker detector layer. However, the background in the energy range from 200 keV to a few MeV is dominated by the telescope internal emission, which increases with the detector volume. A thicker detector will suffer thus an higher background. Therefore, the decision to use only one layer or two layers in coincidence for detecting the photons through the mask, is a trade-off between the detector(s) background level and efficiency.

In another hand, CACT can be used to get the full energy deposit of an high energy photon, even if imaging is done only using the mask projection on one layer. This will enable the users to get an improved energy response of a coded mask telescope.

Lastly, CACT are in general difficult to use at higher energy, near 10 MeV and above, as they would require a thick mask, even with tungsten, to stop the photons, which will result in a large vignetting effect for off-axis sources. Also, at those energies, Compton scatterings and pair creation in the mask will affect the system imaging properties, and may degrade its angular resolution which therefore becomes slightly energy dependant.

In this paper, we present the general principle of CACT, their application to the IN-

TEGRAL mission, the difficulties inherent to the use of CACT, the analysis method of the IBIS Compton Mode and its resulting performance.

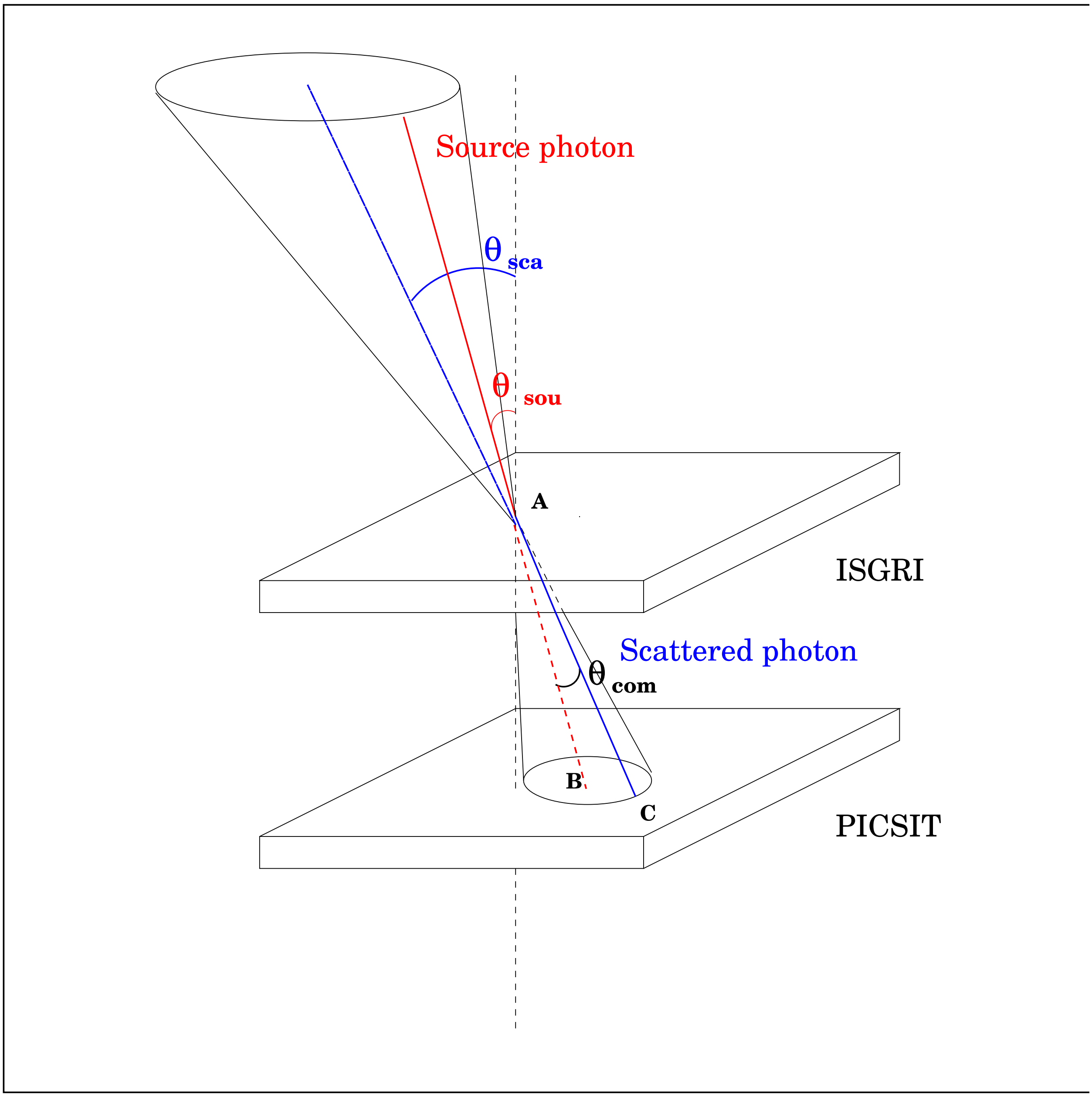

Fig. 1.— Forward scattering of a photon in the IBIS/Compton mode. An incident photon in red is scattered in ISGRI and absorbed in PICsIT (in blue). The energy and position measurements in A and C allow the derivation of the two angles: θ_{com} and θ_{sca}.

2. Principle of a Coded Aperture Compton Telescope

In a Compton telescope, consisting of two detector layers, gamma-ray photons are Compton scattered in one detector and absorbed in the second. The locations and energy deposits of each interaction are measured, as illustrated in Figure 1 for the IBIS detectors. The direction of the scattered photon, $\overrightarrow{u}_{sca}$, is determined from the interaction locations in the two detectors. The Compton scattering angle, θ_{com}, is measured from the energy deposits, E_1 and E_2, recorded in the two detectors and given by, for a forward scattering :

$$\cos\theta_{com} = 1 - \frac{m_e c^2}{E_2} + \frac{m_e c^2}{E_1 + E_2} \tag{1}$$

where $m_e c^2$ is the electron rest mass energy. In a Compton telescope, the direction of the incoming gamma-ray photon lies on the edge of a cone, the Compton cone, with axis $\overrightarrow{u}_{sca}$ and aperture θ_{com}. The density distribution of all the projected event circles, intersection of the cone with the celestial sphere, allows to reconstruct sky maps and to locate sources. Source polarization can also be measured since the scattering azimuth is related to the polarization direction. The angular resolution of the telescope depends on the accuracy of the θ_{com} and $\overrightarrow{u}_{sca}$ determinations and thus depends on the energy resolution and pixel sizes in each of the two detectors. Furthermore, background is hard to subtract and, as in optical cameras, several effects distort images. Using a coded mask to reconstruct sky images effectively addresses most of these difficulties.

In coded aperture telescopes, the source radiation is spatially modulated by a mask of opaque and transparent elements. The projection of the mask shadow recorded with a position sensitive detector produces a shadowgram. This allows simultaneous measurement of source plus background flux (shadowgram area corresponding to the mask holes), and background flux (shadowgram area corresponding to the opaque elements) (Caroli et al. 1987). The background is removed in the deconvolution of the shadowgram using the mask pattern. Mask patterns are designed to allow each source in the field of view to cast a unique shadow on the detector in order to avoid ambiguities in the reconstruction of the sky image. The energy-independent angular resolution is given, in the thin mask limit (see the discussion for thicker masks above), by $d\alpha = arctan(\frac{C}{H})$, where C is the size of a mask element and H is the distance between the coded mask and the detector. In such a telescope the field of view is limited and depends on the mask dimension, the detector dimension and the mask-detector distance. The total field of view is divided in two parts:

- FCFOV (Fully Coded Field Of View) for which the source radiation is completely modulated by the mask. This field exists only when the mask is larger than the detector.

- PCFOV (Partially Coded Field Of View) for which only a fraction of the source radiation is modulated by the mask.

The principle of a CACT takes advantage of both techniques. It is composed of a coded mask and two detector planes between which photons are Compton scattered. The flux on one detector is spatially modulated by the mask pattern. The sky image is obtained by a simple deconvolution of this shadowgram. Compton events that are incompatible with a given source direction can be discarded from the shadowgram, so CACT can be regarded as a coded mask telescope where the Compton kinematics are used to reduce the background.

Then, two cases are possible: Either ones want to study a given source with a known position $\vec{u}_{sou}$ in the celestial sphere or ones wish to make an image of a given field of view. In the first case, we can select, using Compton kinetics, events which fulfill the following condition:

$$\vec{u}_{sou}.\vec{u}_{sca} = cos(\theta_{com}) \tag{2}$$

within instrumental incertainties, as, by definition, θ_{com} is the angle between the source and the scattered directions. In the case of a isotropical background, Eq. 2 enable typically to remove more than 90% of the Compton forward background events, while keeping 90% of the Compton forward source events, in the 200 keV - 1 MeV energy range.

When we want to study sources over a given field of view, the more conservative way of removing background events using the Compton kinetics, is to remove all events whose Compton cones, within uncertainties, do not intersect the field of view. This condition can be readily written in the plane containing the telescope axis and the source direction (for a forward scattering). Indeed, if we consider the case of a conical field of view of semi-angle θ_{FOV}, the selection condition means that the angle between the source direction and the telescope axis $\vec{u}_{tel}$, called θ_{sou}, should be greater than the angle θ_{FOV}. θ_{sou} can be easily computed from the Compton angle and the scattered photon ones (θ_{sca} such as $cos(\theta_{sca}) = \vec{u}_{sca}.\vec{u}_{tel}$). The background rejection condition become then:

$$\theta_{sou} = (\theta_{sca} - \theta_{com}) \geq \theta_{FOV} \tag{3}$$

A similar formula can be obtained in the backward scattering case.

3. The INTEGRAL IBIS/Compton mode

3.1. The IBIS telescope as a CACT

The IBIS instrument (Ubertini et al. 2003) is one of the two major coded aperture telescopes on board the ESA INTEGRAL gamma-ray observatory launched on October 17 2002. It consists of a dual detection layer designed and optimized to operate in the energy range between $\sim$ 15 keV and 10 MeV. The upper detector layer, ISGRI, covering the energy range from $\sim$ 15 keV to 1 MeV, is made of 128×128 Cadmium–Telluride (CdTe) semiconductor detectors (Lebrun et al. 2003). The lower detector layer, PICsIT, operating in the energy interval from $\sim$ 190 keV to 10 MeV, is made of 64×64 Cesium–Iodide (CsI) scintillating crystals (Labanti et al. 2003). Events from these two detection layers are time stamped and an on board Hardware Event Processing Unit (HEPI) can associate the ISGRI and PICsIT events if their arrival times differ by less than a given time coincidence window (actually 3.8 μs). In the following, these events are referred to as tagged Compton events. The detector spectral drifts (gain changes) can be monitored with a ^{22}Na On Board Calibration Unit (OBCU). The detector layers are actively shielded, encased on all but the sky side by bismuth germanate (BGO) scintillator elements. It is also passively shielded from the low energy celestial background with tungsten and lead foils. The coded mask is made of 16 mm thick tungsten elements of 11.2 mm by side. This thickness guarantees a 50% modulation at 1 MeV. Placed 3.2 m above the CdTe detector plane, this mask ensures a 12 arcmin angular resolution over a 29×29 PCFOV. Composed of two detector planes (ISGRI and PICSIT) able to work in coincidence and covered with a coded mask, the IBIS telescope is the first in flight CACT.

3.1.1. Event types

Tagged Compton events from the celestial source under study can be of two kinds:

- true Compton events,
- or spurious events, where two independent ISGRI and PICsIT events, one of them coming from the source, fall by chance in the Compton coincidence time window, and are recorded falsely as a true Compton event.

Below 500 keV, the vast majority of Compton scatters corresponds to forward scattered events (ISGRI $\rightarrow$ PICSIT). With increasing energy, photons can pass through ISGRI without any interaction, interact in PICSIT, and scatter back onto the ISGRI detection layer. In some cases, more than one scattering occurs. Multiple interactions in ISGRI are, however, discarded on board. In this paper we will use only the events that underwent a forward scattering in ISGRI with a single energy deposit in PICsIT.

3.1.2. spectral resolution

In standard Compton telescopes, the spectral resolutions of each detector are key parameters since they directly affect the angular resolution which, in turn, governs the sensitivity. For CACT, the angular resolution is driven by the mask geometrical properties (C and H), but the sensitivity strongly depends on background rejection. The latter is based on measuring $\overrightarrow{u}_{sca}$ and θ_{com}. The uncertainty on θ_{com}, $\delta\theta_{com}$

$$\delta\theta_{com} = \frac{m_e c^2}{E^2 sin\theta} + \sqrt{\delta E_1^2 + \left(\frac{E_1^2}{E_2^2} + 2\frac{E_1}{E_2}\right)^2 \delta E_2^2} \tag{4}$$

where δE_1 and δE_2 are the energy resolution of the first and second detector layers, respectively, is larger in IBIS than that on $\overrightarrow{u}_{sca}$ which relates to pixel size. We have used the Compton data tagged as calibration events by the On Board Calibration Unit to measure the on board spectral resolution of the IBIS Compton mode. The FWHM of the two lines of the ^{22}Na source (511 keV and 1274 keV) and the resulting energy resolution are presented in Table 1.

Table 1: In flight IBIS Compton mode energy resolution

Energy(keV)	Energy resolution (% FWHM)
511	20
1274	15

4. Imaging the sky with the IBIS Coded Aperture Compton Telescope

In this section we focus on imaging analysis and performance of the IBIS/Compton mode.

4.1. The IBIS Compton mode imaging analysis

4.1.1. Events selection

The first step to analyze the IBIS Compton mode data is to apply selections on the events: selection in energy (generally between 200 keV and 1 MeV), and selection of ISGRI events in rise time between 0.6 and 3.8 μs (see Lebrun et al., 2003, for a description of ISGRI data).

Then, we remove background events using the Compton kinetics, as described in paragraph 2. As discussed there, depending on the purpose, there are two types of selection.

- *The field of view selection*: The IBIS field of view semi-angle being $\theta_{FOV} \simeq 15°$, only photons with $\theta_{sca} - \theta_{com} < 15°$ are kept.
- *The dedicated source selection*: for a source of known direction $\overrightarrow{u}_{sou}$, a more restrictive selection given by Eq. 2 is applied. This condition can be rewritten as: $|\overrightarrow{u}_{sou}.\overrightarrow{u}_{sca} - cos(\theta_{com})| < \delta_{lim}$ where δ_{lim} is related to the instrumental error.

We compute values of δ_{lim} in order to maximize the source signal to noise ratio, using ground calibration measures. We have used the Compton events obtained from three on-axis calibration sources, namely ^{133}Sn (392 keV), ^{22}Na (511 keV), and ^{137}Cs (662 keV). In fact, for a on-axis source, the telescope axis and source direction coincide, so

$$\overrightarrow{u}_{sou} = \overrightarrow{u}_{tel} \tag{5}$$

then, from Equation 2, we get

$$cos(\theta_{com}) = \overrightarrow{u}_{sou}.\overrightarrow{u}_{sca} = \overrightarrow{u}_{tel}.\overrightarrow{u}_{sca} = cos(\theta_{sca}) \tag{6}$$

by definition of θ_{sca}. Equation 2 then simplify to :

$$\Delta\theta = \theta_{com} - \theta_{sca} = 0 \tag{7}$$

Figure 2 shows the angular shift $\Delta\theta$ diagrams. This distribution, centered on zero, is not a Dirac distribution because of instrumental incertainties. Also, this distribution narrows with energy due to a better reconstruction of θ_{com}, linked to a better Compton mode energy resolution at high energy. Yet, this variation with energy is small and the optimal choice of δ_{lim} (related to the width of the distribution shown in figure 2) has been checked not to change much with energy between 200 keV and 1 MeV.

Figure 3 illustrates how the signal to noise ratio varies with the allowed range of $\Delta\theta \in [-\theta_{lim}, \theta_{lim}]$ for the ^{133}Sn calibration source. The best value of θ_{lim} at 392 keV is around $10 - 12°$.

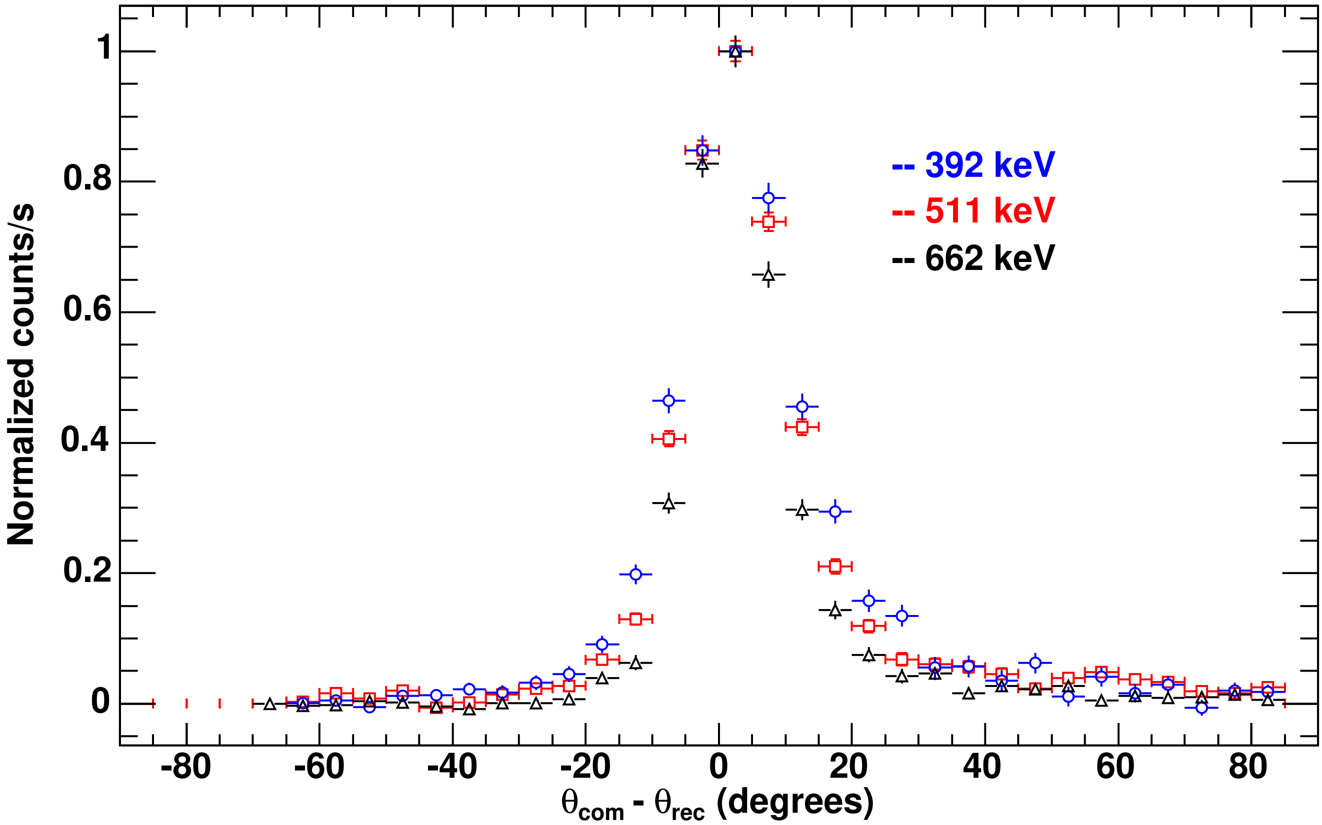

Fig. 2.— Distribution of Compton events with the angular shift $\Delta\theta = \theta_{com} - \theta_{sca}$, after spurious events removal, using on-ground calibration data from ^{133}Sn ($392keV$), ^{22}Na ($511keV$), ^{137}Cs ($662keV$) sources (θ_{rec} in this figure is equal to θ_{sca} in the text).

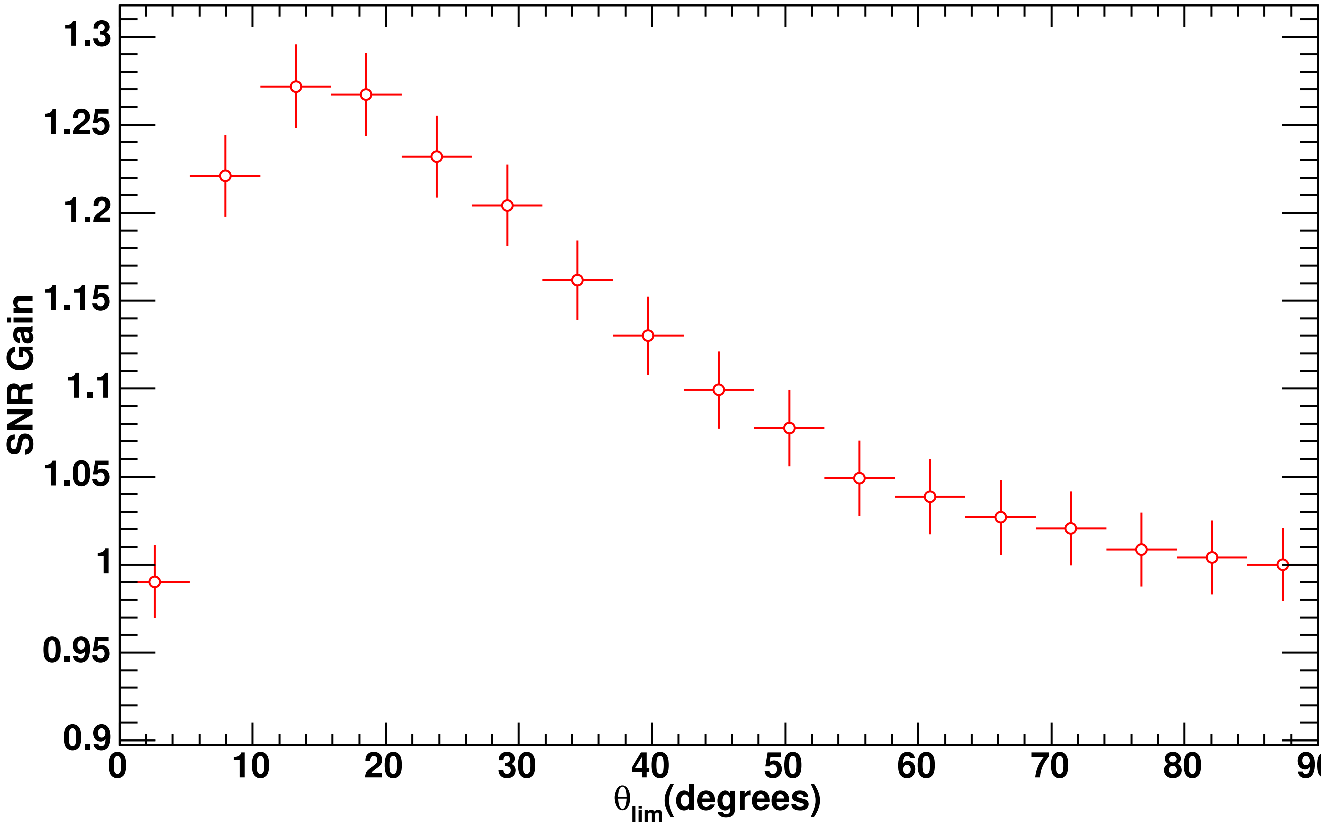

Fig. 3.— Evolution of the signal to noise ratio gain with θ_{lim} for the ^{133}Sn calibration source at 392 keV on axis.

4.1.2. Spurious events subtraction

Spurious events are generally neglected in standard Compton telescopes. Their uniform distribution does not induce false source detection. But the situation for CACT is different:

Indeed, spurious events are composed by random events on the two layers. For a bright source, like Crab, the source low energy photons have a important contribution in the detectors count rates. So, the probability that one of these random events is in fact a detected low energy photon from the source is quite high. As this photon has the mask signature induced by the source, it is not subtracted during the deconvolution process, and wrongly participate to the source flux determination. So, we have to take into account the spurious events contribution with high accuracy in order to get a correct estimate of the source flux.

The dedicated source selection has the strong advantage of largely reducing the number of spurious events, as most of them does not obey Equation 2, but their remaining contribution is not negligible. A statistical method must be applied to evaluate and subtract them.

To do so, we make use of the ISGRI and PICSIT single events recorded in the same observation, that is possibly having the source signature, to artificially associate them and create a sample of spurious events, called hereafter the "fake spurious events sample". We apply to this sample the same selections in energy, rise time, and scattering angle as described above in order to produce a fake shadowgram. The latter is scaled, by a scaling factor called hereafter "spurious factor" or "α", to the number of spurious events recorded during the observation and then subtracted from the Compton data shadowgram.

The spurious count rate, N_{Sp} scales with the width of the time coincidence window ($\sim 2\Delta T_e$), the total number of PICSIT events ($N_{PICSIT} = N_P + N_{OBCU}$ from PICSIT simple and multiple detections, and from calibration events), and the total number of ISGRI events ($N_{ISGRI} = N_I + N_{Sp}$ from ISGRI single events and spurious events). The calibration events in ISGRI are tagged and discarded on board. Using Poisson statistics in the coincidence window, one obtains the number of spurious events:

$$N_{Sp} = (1 - e^{-(2\Delta T_e - \delta T)(N_{PICSIT})})N_{ISGRI} \tag{8}$$

where δT is the on-board time resolution, of the order of 250 ns. Yet, one measures only N_I, so the scaling factor is

$$N_{Sp}/N_I = (e^{(2\Delta T_e - \delta T)(N_{PICSIT})} - 1) \tag{9}$$

One has to further correct this factor for the multiple PICSIT events in order to get the scaling factor for the single spurious events only. For a proportion of PICSIT single events of

$$\beta = \frac{N_P^{simple} + N_{OBCU}}{N_P^{simple} + N_P^{multiple} + N_{OBCU}} \tag{10}$$

(β is of the order of 80% between 200 keV and 1 MeV for IBIS), one gets the spurious factor

$$\alpha = \beta(e^{(2\Delta T_e - \delta T)(N_{PICSIT})} - 1) \tag{11}$$

Figure 4 shows the evolution of the spurious factor for Crab observations through the mission lifetime. It varies from 2.82 % early in the mission (revolution 39) when ΔT was about 5.0 μs, to around 1.1 % after revolution 102 when ΔT_e was decreased to 1.9 μs. α is quite constant for a given coincidence window during a short time, but rises on longer periods (Rev. $102 - 103 - 170 - 239$), due to the increase of the background flux, following the solar cycle.

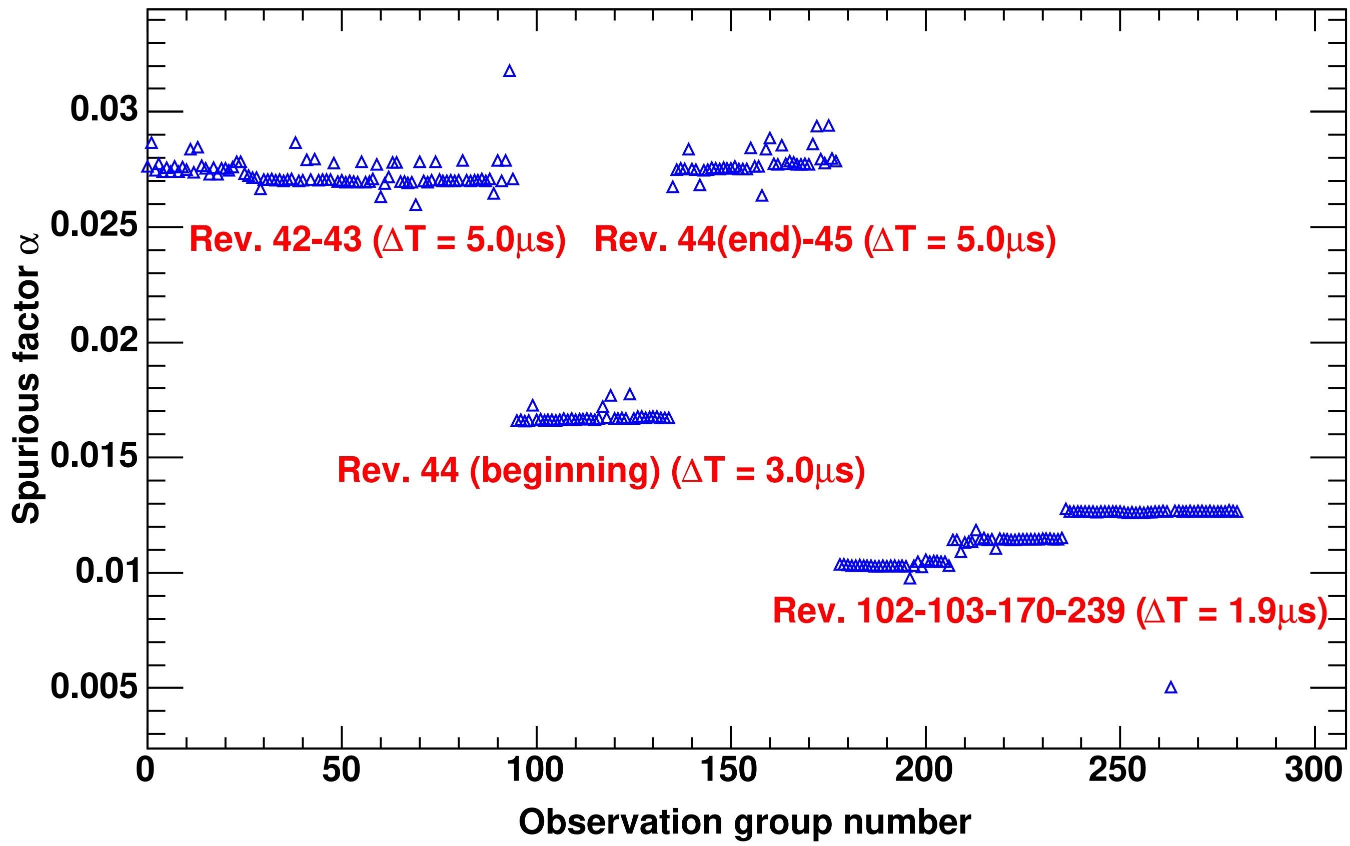

Fig. 4.— Evolution of the spurious factor for different values of the time coincidence window as derived from Crab pulsar observations.

The next step is to correct the resulting shadowgram (after subtraction of the spurious events) for its non-uniformity and to deconvolve it.

4.1.3. Uniformity correction

Compton mode shadowgrams are not spatially flat. The count rate falls near the edges because we lose the events which scatter at the edge of ISGRI and miss PICSIT. This non-uniformity is magnified by the decoding process so, if not corrected, strong systematic structures may result in the deconvolved images with spatial frequencies similar to those originally present in the shadogram. The shadowgram, D, consists of a source component, with count rate S and a spatial response map R_S, and a background component, with count rate B and response map R_B, thus

$$D = S \times R_S + B \times R_B \tag{12}$$

The modulation from the mask pattern is weak compared to the larger scale deformations we study here. To compare R_S and R_B in the same conditions, we need in-flight data from a source strong enough as well as background. Whereas we have used the in-flight background distribution, there is no such source observed in-flight in Compton mode, so we used data from on-ground calibration to determine R_S.

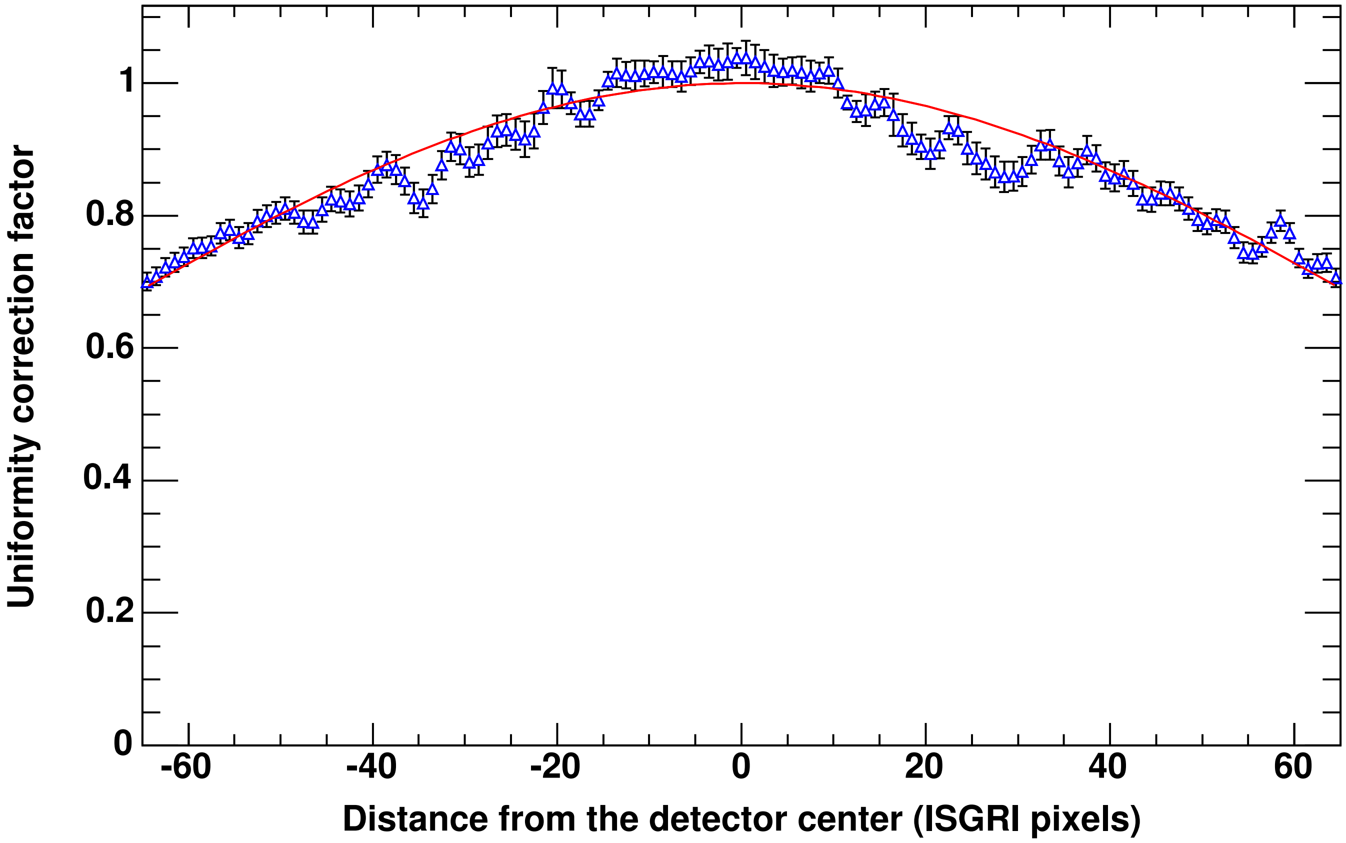

Fig. 5.— Distribution of background events with distance from the detector center, folded over the azimuthal direction. This distribution is well fitted by a 2D gaussian shown in red.

Both the background and source response maps are well fitted by a 2D gaussian function (see Figure 5). The results are presented in Table 2 for the in-flight background measurements and the on-ground calibration source data for on-axis sources. The background and source response maps in several energy bands are found to be consistent. Off-axis sources have also been studied and display equivalent response maps.

Table 2: response maps gaussian fits

Source	Energy(keV)	σ(pixels)
^{113}Sn	392	73 ± 3
^{22}Na	511	74 ± 3
^{137}Cs	662	71 ± 4
^{54}Mn	835	72 ± 2
^{54}Zn	1120	73 ± 3
Background	$200 - 5000$	74 ± 3

Residual background deformations on smaller scales, similar what is observed in ISGRI images (Terrier et al. 2003), are still present; their correction is under study.

The final step is therefore to deconvolve the corrected shadowgram D/R, renormalized to the total number of events, to reconstruct the source flux, using standard deconvolution techniques.

4.1.4. Image deconvolution

Representing the mask with an array M of 1 (transparent) and 0 (opaque) element, the detector plane by an array D, and denoting by G^{+} and G^{-} the decoding arrays related to the coded mask (see (Goldwurm et al. 2003)), the image deconvolution in the fully coded field of view (FCFOV) can be extended to the total (fully coded and partially coded) by performing the correlation of D in a non cyclic form with the G array extended and padded with 0 elements outside the mask (Gros et al. 2003). Since the number of correlated (transparent and opaque) elements in the partially coded field of view is not constant as in the FCFOV, the sum and subtractions for each sky position must be balanced and renormalized. The sky flux map is given by :

$$F = \frac{(WD * G^{+}) - (WD * G^{-})\frac{(W*G^{+})}{(W*G^{-})}}{(W * G^{+}M) - (W * G^{-}M)\frac{(W*G^{+})}{(W*G^{-})}} \tag{13}$$

and the variance map by:

$$V = \frac{(W^{2}D * G^{+2}) + (W^{2}D * G^{-2})(\frac{(W*G^{+})}{(W*G^{-})})^{2}}{((W * G^{+}M) - (W * G^{-}M)\frac{(W*G^{+})}{(W*G^{-})})^{2}} \tag{14}$$

In the previous formulae, the W matrix removes dead or noisy pixels.

In the FCFOV, the variance is quite uniform and equals the total number of detector counts. All this analysis procedure can be easily carried out by means of Fast Fourier transforms. The result on a Crab pulsar observation is presented on Figure 6.

On Figure 7, on the left, we show for comparison an ISGRI alone significance map, in the same energy range. As expected, due to its low thickness (2 mm), ISGRI is much less sensitive that the Compton mode between 200 keV and 500 keV, showing that the Compton mode is a real extension at high energy of the ISGRI capabilities. On Figure 7, on the right, we show the significance map made with the fake spurious events sample, using the same algorithms as the ones used for Figure 6. It is clear there that this map is dominated by low energy events coming from the Crab, as described in part 4.1.2.

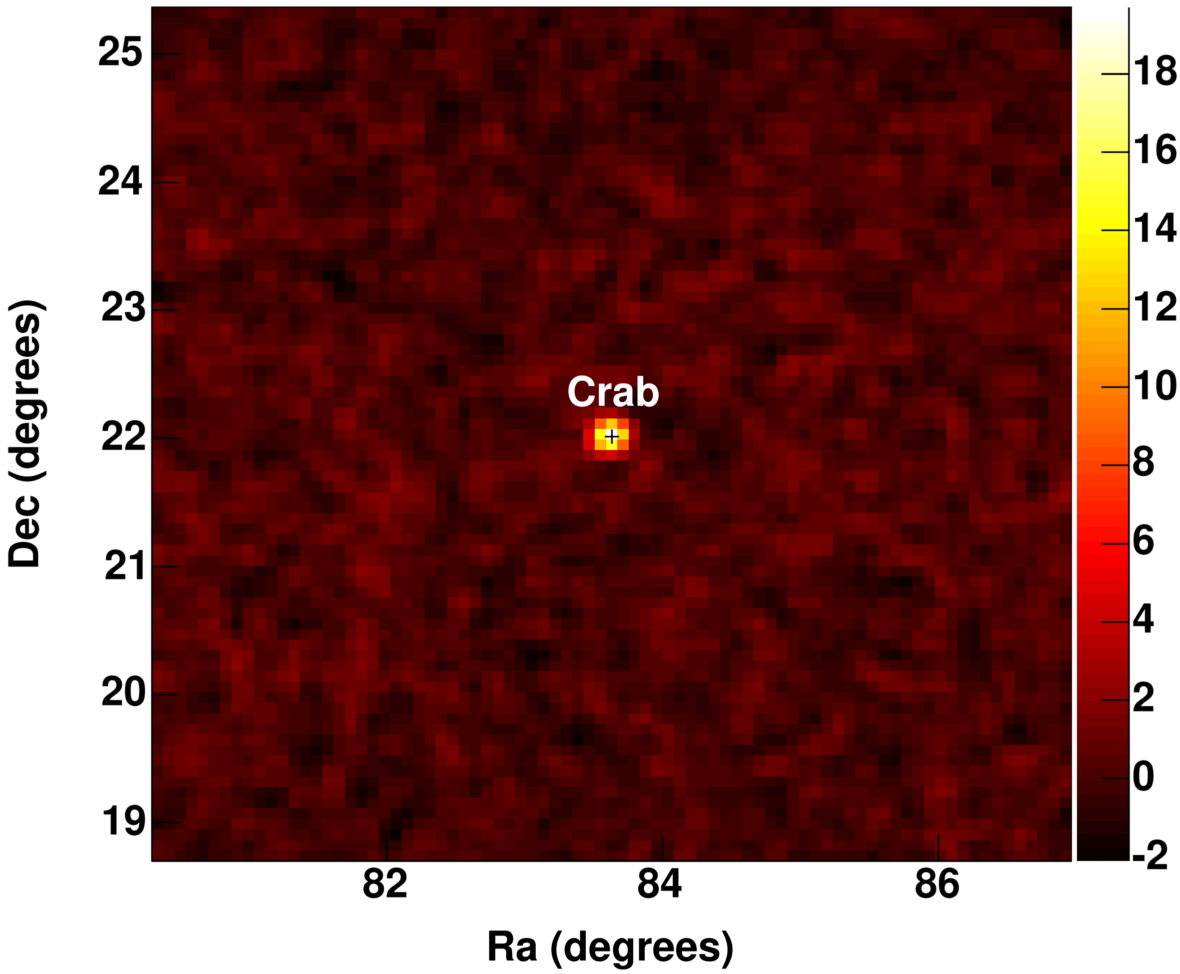

Fig. 6.— Deconvolved significance map for the Crab pulsar using the Compton mode between 200 keV and 500 keV for an exposure time of 300 ks.

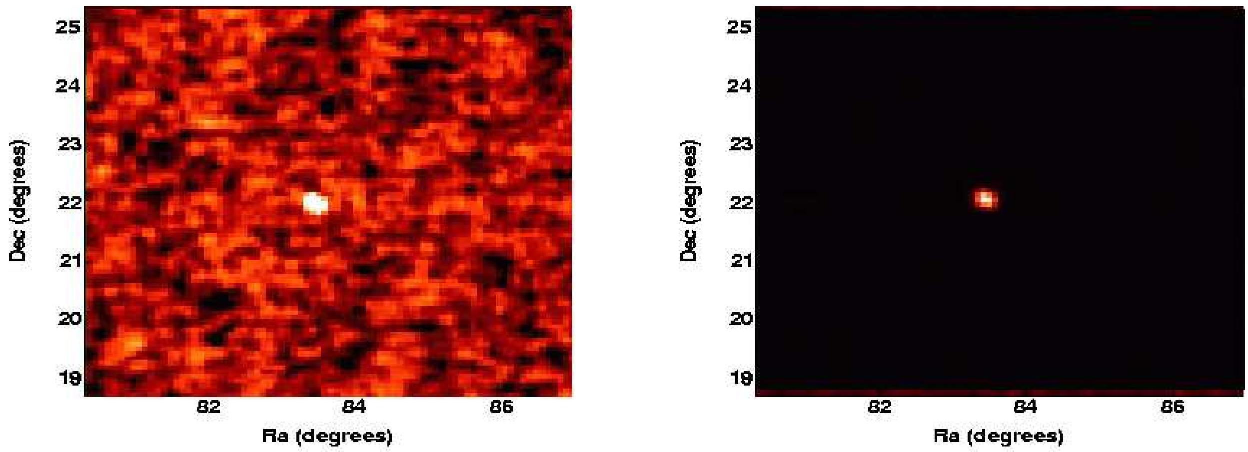

Fig. 7.— left: ISGRI significance map of the Crab pulsar between 200 keV and 500 keV. right: Significance map computed from the fake spurious events sample, and computed with the same algorithms as used for the map shown in Figure 6.

4.1.5. Angular shift diagrams as a check for the analysis method

Angular shift diagrams illustrate the effectiveness of the spurious event subtraction. One can use Compton tagged events from an on-axis calibration source and analyze them in regularly spaced $\Delta\theta$ bins. Then we select them in energy and rise time as above. Their shadowgram are corrected for the spatial response and deconvolved to get the total source count rate displayed in red in Figure 8. The corresponding constructed spurious event sample has been analyzed in the very same way and its count rate per $\Delta\theta$ bin, scaled by the measured α factor, is displayed in blue, showing that the spurious factor is adequate. The angular shift $\Delta\theta$ distribution of real Compton events (after subtraction of the spurious ones) is well centered around zero and fall to zero for $|\Delta\theta| \geq 19°$ whereas the spurious distribution is clearly offset to negative values, as expected because most spurious events have a low energy deposit in ISGRI.

For celestial γ-ray sources above 200 keV, the spurious rate dominates over the source rate. Several Crab on-axis observations have been used to construct a $\Delta\theta$ diagram, using the variance weighted sum of the flux at the source position in each sky image. Thanks to the coded mask background subtraction capabilities, only the true Compton and spurious contributions as defined in section 3.1.1, are visible on Figure 9. The spurious component severely dominates, its negative offset being well marked. True Compton events are around zero, as foreseen, and the small flux excess of events for $\Delta\theta \sim 20° - 40°$ is due to backward scattered events.

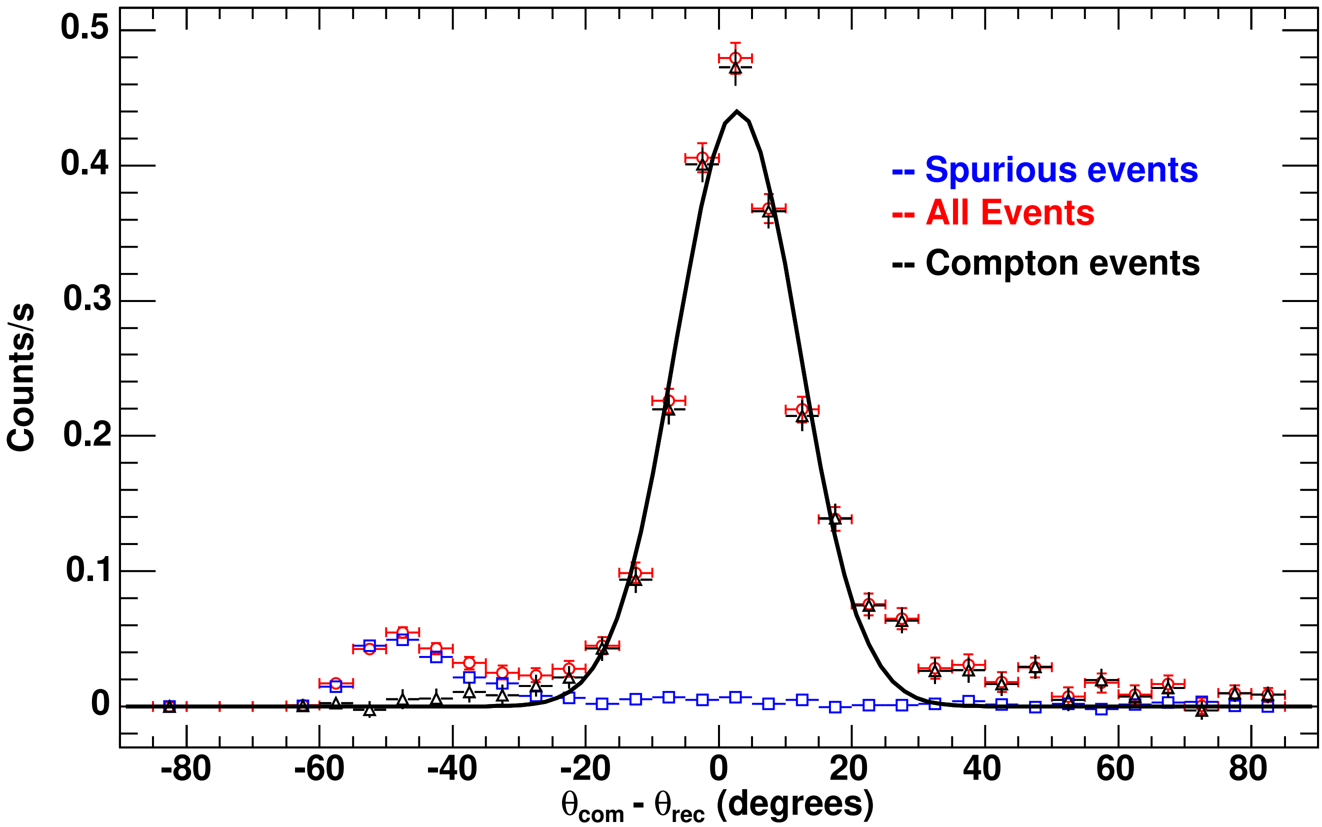

Fig. 8.— Angular shift distribution of events for a calibration source of ^{133}Sn at 392 keV during on ground calibration. Red data points represent all the Compton data (real Compton plus spurious data). Blue data points show the spurious contribution, which peaks at negative offset, and black data points are the derived Compton ones. The line is a gaussian fit ($FWHM \sim 19°$) to this derived Compton data.

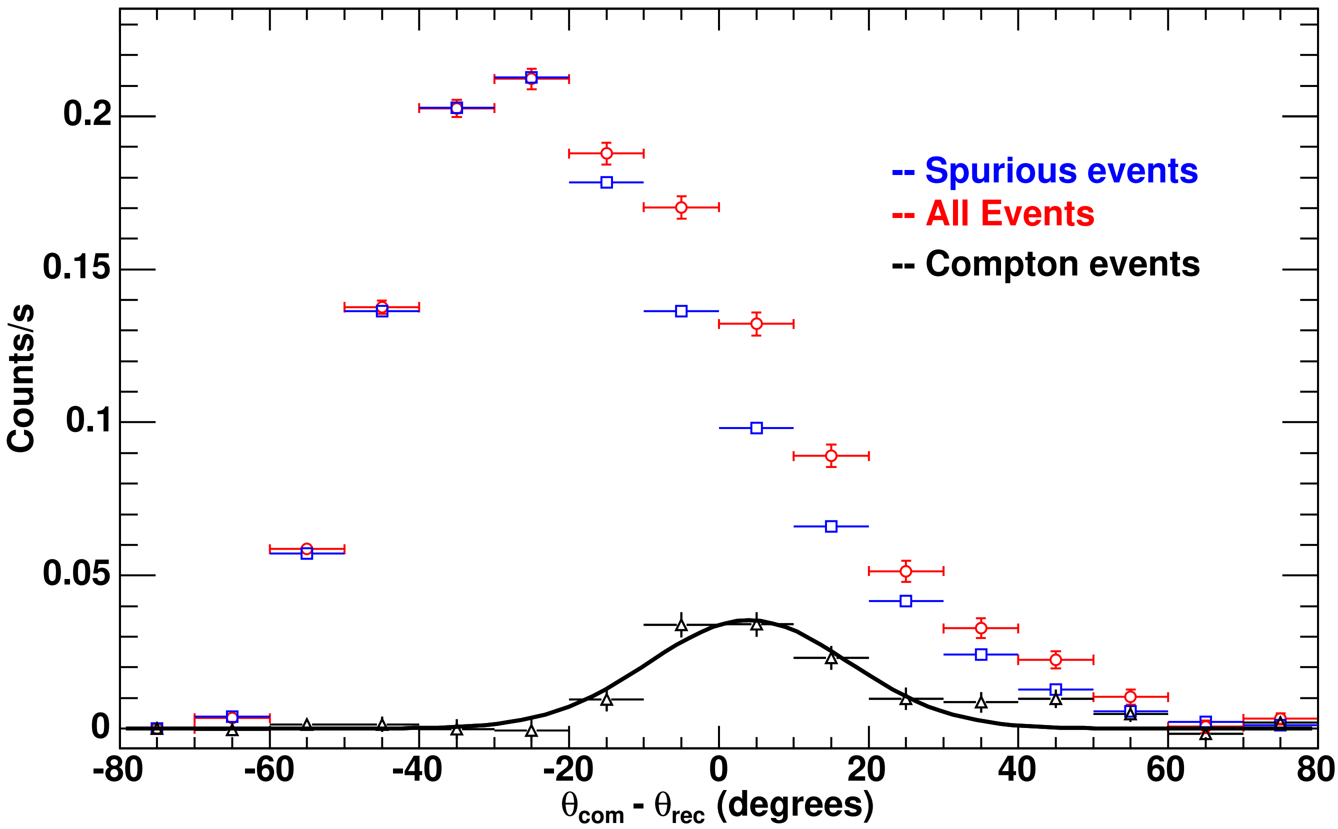

Fig. 9.— Crab count rate between 200 keV and 500 keV in different $\Delta\theta$ bins. The total observation time is about 700 ks. Red data points represent all the Compton data (real Compton plus spurious data). Blue data points show the spurious contribution, and black data points are the derived Compton ones. The line is a gaussian fit to the Compton data.

4.2. The IBIS Compton mode sensitivity

The analysis method described above has been applied to evaluate the signal to noise ratio of the Crab pulsar in different energy bands. The sensitivity of the IBIS Compton mode is presented on Figure 10. It is greater than that of PICSIT for a similar angular resolution. Yet, unlike PICSIT, the Compton mode has no major strong background problems, allows to study photons up to a few MeV in very small energy bands, in particular around spectral lines, with an angular resolution better than that of SPI. It also allows to perform polarization studies and imaging studies of compact objects with a good timing resolution ($\sim 100\mu s$).

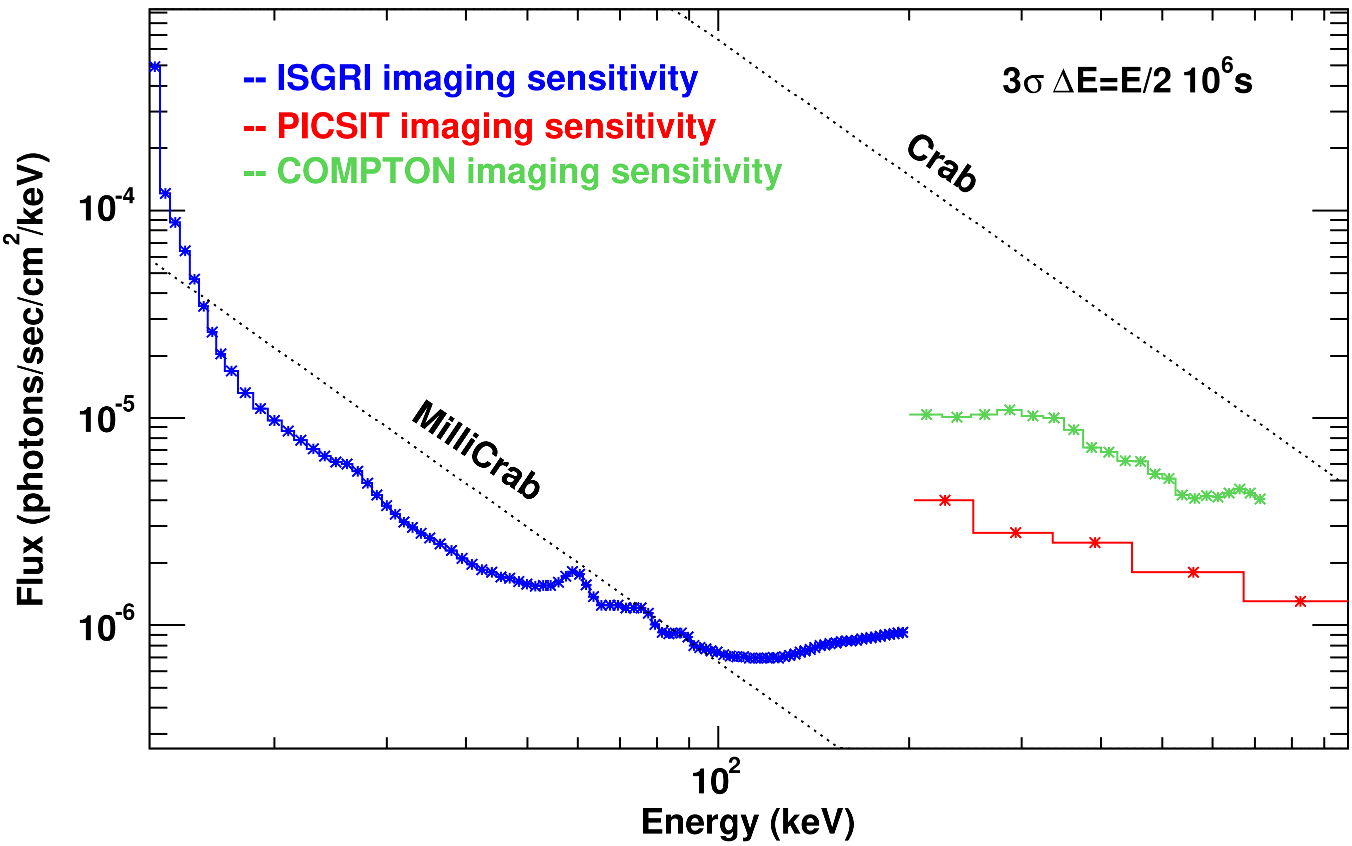

Fig. 10.— Sensitivity of the IBIS Compton mode compared to the ISGRI and PICSIT sensitivity.

The next step we foresee in our analysis is to incorporate backward scattered events, PICSIT multiple events, and compute background Compton correction maps (first order background shadowgram from empty field observations and second order summed sky images after source subtraction) to reduce the residual structures in the response maps.

An important goal of the IBIS Compton mode is also polarimetry. The interest of the astrophysics community to such detection is growing. It is in fact a powerful and a direct tool to constrain theoretical model on GRB, pulsars, solar flares, etc.

The calibration and results of the IBIS Compton mode polarimeter will be presented in a forecoming paper.

5. Conclusions

The IBIS Compton mode is functional and provides a new efficient means to observe the sky at energies beyond $\sim$ 190 keV up to a few MeV. With only forward scattered events and thus thanks to the ISGRI shadowgram, we can reconstruct images with high spatial resolution taking advantage of the coded mask aperture system. We have devised a scheme for subtracting the large contribution from spurious coincidences between the two detector planes. The resulting sensitivity, evaluated with in-flight data from the Crab pulsar, opens new perspectives for polarimetric and imaging studies in the 0.2-5 MeV energy band.

We thank the anonymous referee for interesting questions and helpful suggestions that significantly improved the whole paper.

REFERENCES

Boggs, S.E., & Jean, P. 2000, A&AS, 145, 311

Caroli, E., Stephen, J.B., di Cocco, G., Natalucci, L., & Spizzichino, A. 1987, Space Science Reviews, 45, 349

Diehl, R., et al. 1995, A&A, 298, 445

Goldwurm, A., et al. 2003, A&A, 411, L223

Gros, A., Goldwurm, A., Cadolle-Bel, M., Goldoni, P., Rodriguez, J., Foschini, L., Del Santo, M., & Blay, P. 2003, A&A, 411, L179

Herzo, D., et al. 1975, Nucl. Inst. Meth., 123, 583

Labanti, C., et al. 2003, A&A, 411, L149

Lebrun, F., et al. 2003, A&A, 411, L141

Limousin, O. 2003, Nuclear Instruments and Methods in Physics Research A, 504, 24

Lockwood, J. A., Hsieh, L., Friling, L., Chen, C., & Swartz, D. 1979, J. Geophys. Res., 84, 1402

Terrier, R., et al. 2003, A&A, 411, L167

Ubertini, P., et al. 2003, A&A, 411, L131

Schönfelder, V., et al. 1993, ApJS, 86, 657

Schönfelder, V., & Lichti, G. 1973, International Cosmic Ray Conference, 4, 2709

Zoglauer A., & Kanbach G. 2003, SPIE, 4851, 1302